On the use of simulated experiments in designing tests for material characterization from full-field measurements

Marco Rossi, Fabrice Pierron

LMPF, Arts et Métiers ParisTech, Rue St Dominique, B.P.508, 51006
Châlons-en-Champagne, France, email: marco.rossi@ensam.eu,
Fabrice.Pierron@chalons.ensam.fr

Abstract

The present paper deals with the use of simulated experiments to improve the design of an actual mechanical test. The analysis focused on the identification of the orthotropic properties of composites using the unnotched Iosipescu test and a full-field optical technique, the grid method. The experimental test was reproduced numerically by finite element analysis and the recording of deformed grey level images by a CCD camera was simulated trying to take into account the most significant parameters that can play a role during an actual test, e.g. the noise, the failure of the specimen, the size of the grid printed on the surface, etc. The grid method then was applied to the generated synthetic images in order to extract the displacement and strain fields and the Virtual Fields Method was finally used to identify the material properties and a cost function was devised to evaluate the error in the identification. The developed procedure was used to study different features of the test such as the aspect ratio and the fibre orientation of the specimen, the use of smoothing functions in the strain reconstruction from noisy data, the influence of missing data on the identification. Four different composite materials were considered and, for each of them, a set of optimized design variables was found by minimization of the cost function.

Preprint submitted to Int. J. Solids Struct. *May 2, 2011*

Keywords:
Simulated experiments, Full-field measurements, Material characterization, Test optimization

---

1. Introduction

The characterization of the mechanical properties of materials by experimental tests is one of the important issues in engineering. Depending on the type of material and the property to determine, many different tests have been devised during the years, some of which have become standards in industrial practice. Looking at mechanical properties, such as elastic modulus, Poisson's ratio, yield strength, toughness, damage, etc., the experimental procedure usually consists in submitting a specimen to different loading conditions and measuring the applied force and specimen deformation. Examples of this kind of experiments are tensile tests, upsetting tests, shear tests, punch tests, bulge tests, etc. When the material behaviour is more complex and several parameters must be identified in the constitutive equation, as occurs for instance in composites, anisotropic metals or rubbers, the characterization becomes more difficult and multiple tests have to be used.

Recently, the improvement in full-field measurement techniques and digital camera performances has led to the design of novel test procedures (Avril et al., 2008a; Grédiac, 2004). The idea is to use a test configuration that induces heterogeneous stress and strain fields in the specimen so that more parameters of the material constitutive equations can be activated at the same time. The full-field measurement technique is employed to measure the displacement field of the specimen surface. At this point, the measured data are used to identify the material properties by inverse approaches, e.g. the finite element updating method (Cooreman et al., 2008; Lecompte et al., 2007; Le Magorou et al., 2002; Meuwissen et al., 1998; Kajberg and Lindkvist, 2004), the constitutive equation gap method (Latourte et al., 2008; Geymonat and Pagano, 2003), the equilibrium gap method (Claire et al., 2004), the reciprocity gap method (Bui et al., 2004) or other techniques (Rossi et al., 2008).

An alternative is the Virtual Fields Method (VFM) which is a well established technique to characterize the material properties directly from full-field measurements (Grédiac et al., 2006). A number of different applications have already been considered in past studies, e.g. the elastic stiffness of composites (Grédiac and Vautrin, 1990; Moulart et al., 2006), damping measurements on vibrating plates (Giraudeau and Pierron, 2005), elasto-plasticity (Grédiac and Pierron, 2006) etc.

The pattern of the displacement field generated by the experiment and the optical technique adopted to measure it play an important role in the final identification of the parameters. The intention of this paper is to develop a procedure to design an optimized test configuration for a given class of materials and type of test. This has scarcely been addressed in the literature (Le Magorou et al., 2002; Pierron et al., 2007; Syed-Muhammad et al., 2009) and a lot of improvements can still be made in this field.

The best configuration comes from the minimization of a cost function that represents the average error in the identification as a function of the design variables. It is not practically feasible to use real experiments in the optimization process because of the great amount of different configurations that have to be tested and the difficulty of controlling the experimental conditions. For this reason the experiments have been simulated using a combination of FE models and data post-processing. A great attention is necessary on reproducing real experiments to avoid the presence of numerical artifacts that could lead to unexpected results. Similar procedures were already used, for instance, to assess the error in digital image correlation measurements with simulated white-light speckle patterns (Bornert et al., 2009).

In this paper, the study focused on the unnotched Iosipescu test (Pierron and Grédiac, 2000) used to determine the constitutive parameters of orthotropic materials such as carbon or glass epoxy composites. The four in-plane stiffness components can be determined from one test using the VFM. A first attempt to optimize the test configuration of a Iosipescu test was addressed in a previous paper by Pierron et al. (2007) where the sensitivity to noise was used as the variable to minimize a cost function. Although an improvement in the quality of the identification was obtained, some limitations were noticed in such an approach. Mainly, the optimization procedure did not include the effect of the spatial resolution of the measurement technique, besides, only one source of error was considered, the uncorrelated white noise on the strain field.

The present work represents a continuation and an extension of that study. In order to overcome the mentioned limitations, the intent here is trying to numerically reproduce the whole measurement process as accurately as possible. Synthetic images were generated to simulate a real acquisition with a CCD camera and the noise was applied directly to the grey level images. A full-field technique, the grid method, was used to extract the strain field from the images and the data were used to identify the parameters with the VFM. In this way the effect of the spatial resolution is introduced and the influence of noise is more realistic.

The developed procedure gives a versatile tool to study and optimize an experimental setup and several practical aspects can be efficiently evaluated, for instance the effect of smoothing procedures to derive the strains from the displacements or the influence of missing data, two very important practical features. Moreover the same procedure could be easily extended to take into account other important aspects like the existence of optical distortions or the pixel fill factor.

To the best knowledge of the authors, this is the first time that the whole measurement and identification chain is simulated and used to optimize a test configuration.

2. Description of the techniques used in the simulated experiments

The identification process is based on two specific techniques, the grid method, used to measure a two-dimensional displacement field on a loaded specimen, and the Virtual Fields Method, used to identify the material properties from full-field measurements. An in-depth treatment of the subject can be found in the cited references, nevertheless a brief description of the methods is given below to provide a background for the reader and produce a better understanding of the following sections.

2.1. The grid method

The grid method is a full-field optical technique that allows to measure the displacement field on a specimen surface with a high resolution and therefore it is particularly suitable for the small displacements obtained in the elastic range (Avril et al., 2004a,c; Surrel, 1994).

A grid pattern is printed onto the surface of the specimen using appropriate techniques (Piro and Grédiac, 2004) and a digital image of the surface is achieved using a CCD camera. The intensity of the digitized light at a given pixel M_0, that corresponds to the material point determined by the position vector $\overrightarrow{R}(x, y)$ in the reference cartesian frame, can be expressed by:

$$I\left(\overrightarrow{R}\right) = I_0 \left\{1 + \gamma \text{frng}\left[2\pi \overrightarrow{F} \cdot \overrightarrow{R}\right]\right\} \tag{1}$$

where

- I_0 is the local intensity bias,
- γ is the contrast,
- frng is a 2π-periodic continuous function,
- $2\pi \overrightarrow{F} \cdot \overrightarrow{R}$ is the phase of function frng,
- $\overrightarrow{F}$ is the spatial frequency vector. It is orthogonal to the grid lines and its amplitude is the spatial frequency of the grid. If the grid lines are vertical (parallel to the y-axis), the spatial frequency vector writes $\overrightarrow{F}\,(f_0, 0)$. If the grid lines are horizontal, the spatial frequency vector writes $\overrightarrow{F}\,(0, f_0)$.

When a load is applied, the material and consequently the grid are deformed. The phase of the function frng at pixel M_0 varies of $-2\pi \overrightarrow{F} \cdot \overrightarrow{u}(\overrightarrow{R})$ from the undeformed to the deformed state, where $\overrightarrow{u}(\overrightarrow{R})$ is the displacement vector. The $u_x\,(x, y)$ and $u_y\,(x, y)$ displacement components relative to the unloaded reference condition are calculated from the respective phase differences $\Delta\phi_x$ (for vertical lines) and $\Delta\phi_y$ (for horizontal lines) introduced by the deformation:

$$u_x\left(x,y\right) = -\frac{p}{2\pi}\Delta\phi_x\left(x,y\right) \tag{2}$$

$$u_y\left(x,y\right) = -\frac{p}{2\pi}\Delta\phi_y\left(x,y\right) \tag{3}$$

with p equal to the pitch size of the grid. It has to be pointed out that the grid method and the computation of the displacement using Eq. 2 and 3 is valid only under the hypothesis of small displacement. The strain field is obtained consequently by a differentiation of the displacement field:

$$\varepsilon_{ij} = \frac{1}{2}\left[\frac{\partial u_i}{\partial x_j} + \frac{\partial u_j}{\partial x_i}\right]; i, j \in [1-3] \tag{4}$$

Routines to extract the phase fields by using the spatial phase shifting method, *i. e.* the Windowed Discrete Fourier Transform (WDTF) algorithm with a triangular window, have been already implemented in Matlab and can be directly applied to the digital images (Surrel, 1996, 1997). Considering the first harmonic of function frng, Eq. 1 has three unknowns, so a minimum sampling of 3 pixels per period is necessary. The practical experience demonstrated that a good compromise is to have the period p of the grid sampled by about five pixels. Increasing the number of pixels per period will reduce the spatial resolution while going under five pixels will start to deteriorate the phase detection.

Another practical issue is the minimum size of the grid which is possible to print on the specimen. Although microgrids have been successfully used for measurements at the microscale (Moulart et al., 2007, 2009), in applications at the macroscale level the minimum grid pitch is around 100 μm (Piro and Grédiac, 2004), which is the value adopted here. Most of the full-field optical techniques have similar problems, for example, using digital image correlation on white light speckles the ultimate spatial resolution is equal to the size of the correlation subset (Bornert et al., 2009), however, practically, the size of the correlation subset is limited by the minimum size of the speckles painted onto the specimen surface.

2.2. The virtual fields method (VFM)

The VFM is based on the principle of virtual work that, for a solid of any shape of volume V and boundary surface ∂V, in the case of small perturbations and absence of body forces, can be written as:

$$\int_V \underline{\underline{\sigma}} : \underline{\underline{\varepsilon}}^* dV = \int_{\partial V} \overrightarrow{F} \cdot \overrightarrow{u^*} dS \tag{5}$$

where $\underline{\underline{\sigma}}$ is the stress tensor, $\overrightarrow{F}$ the surface forces acting at the boundary, $\overrightarrow{u^*}$ a kinematically admissible virtual field and $\underline{\underline{\varepsilon^*}}$ the corresponding virtual strain field. In the case of an in-plane test, if t is the constant thickness of the volume V and S the planar surface, the problem reduces to a 2-D situation and Eq. 5 becomes:

$$t \int_S \underline{\underline{\sigma}} : \underline{\underline{\varepsilon}}^* dS = t \int_{\partial S} \overrightarrow{F} \cdot \overrightarrow{u^*} dl \tag{6}$$

The constitutive equation for linear orthotropic materials, using the conventional notation for contracted indices $xx \to x$, $yy \to y$, $xy \to s$, writes:

$$\begin{pmatrix} \sigma_x \\ \sigma_y \\ \sigma_s \end{pmatrix} = \begin{bmatrix} Q_{xx} & Q_{xy} & 0 \\ Q_{xy} & Q_{yy} & 0 \\ 0 & 0 & Q_{ss} \end{bmatrix} \begin{pmatrix} \varepsilon_x \\ \varepsilon_y \\ \varepsilon_s \end{pmatrix} \tag{7}$$

$\underline{\underline{Q}}$ is the in-plane stiffness matrix and the four independent components are the parameters to be identified. The stress tensor in Eq. 6 can be rewritten in terms of the strain tensor using Eq. 7:

$$Q_{xx}\int_S \varepsilon_x\varepsilon_x^* dS + Q_{yy}\int_S \varepsilon_y\varepsilon_y^* dS + Q_{xy}\int_S \left(\varepsilon_x\varepsilon_y^* + \varepsilon_y\varepsilon_x^*\right) dS + \\ Q_{ss}\int_S \varepsilon_s\varepsilon_s^* dS = \int_{\partial S} F_x u_x^* dl + \int_{\partial S} F_y u_y^* dl \quad (8)$$

At this point, introducing four independent virtual fields in Eq. 8, four linear equations are obtained that can be used to identify directly the four unknown parameters Q_{xx}, Q_{yy}, Q_{xy} and Q_{ss}. The strain components ε_x, ε_y and ε_s are measured on the specimen surface using a full-field optical technique, and in order to solve the system, the virtual displacements have to be chosen in such a way that the only information involved in the second term of Eq. 8 is the global load measured by the load cell of the experimental equipment.

In the specific case of the unnotched Iosipescu test, the area S of Eq. 8 is the dashed area in the schematic view of Figure 1. The virtual fields have to fulfil the following virtual boundary conditions:

$$\left\{\begin{array}{l} u_x^* = 0 \\ u_y^* = 0 \end{array}\right|_{x=0} \quad \text{and} \quad \left\{\begin{array}{l} u_x^* = 0 \\ u_y^* = c \end{array}\right|_{x=L} \quad (9)$$

where c is a constant. Under these conditions, the only boundary force involved in the second term of Eq. 8 becomes F_y when $x = L$, multiplied by a constant. The constant c can be taken out of the integral and the integral of F_y along ∂S returns the total force F applied to the moving clamp divided by the thickness. The total force can be experimentally measured by a load cell. More details are given in Pierron and Grédiac (2000).

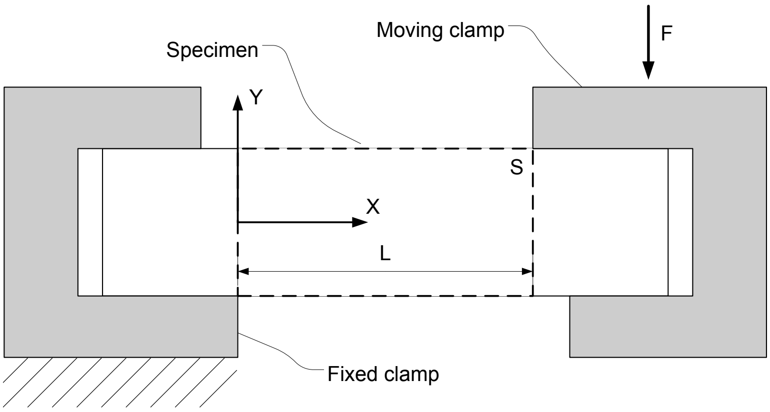

Figure 1: Schematic view of the unnotched Iosipescu test.

An infinite number of virtual fields which satisfy the boundary conditions can be found. The choice of appropriate virtual fields is one of the critical points of the method and has been discussed in several papers (Grédiac et al., 2002a,b). In the present work the approach proposed by Avril et al. (2004b) is used, where a set of optimized virtual fields can be automatically generated by minimizing the sensitivity to noise.

3. Simulated experiments

The simulated experiment is the unnotched Iosipescu test, performed according to the experimental configuration described in Pierron et al. (2007) and Chalal et al. (2006). A finite element model of this test was developed and the computed displacement field was used to reconstruct synthetic images that simulate an actual acquisition with a CCD camera. The whole process will be discussed in details.

3.1. *Finite elements simulations*

A parametric model was built up using ABAQUS Standard and Python routines, all the simulations can be run in background under a Matlab environment and easily inserted in optimization programs.

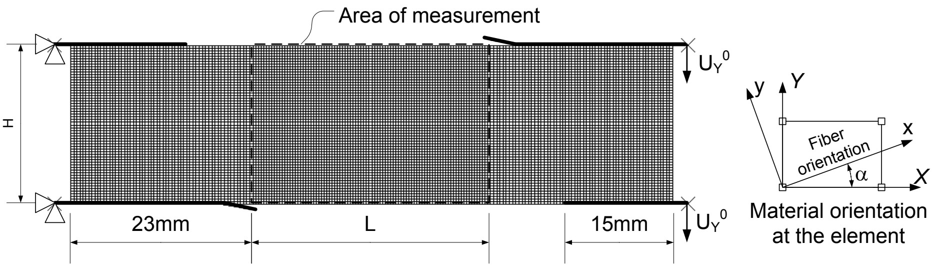

Figure 2: FEM model of the unnotched Iosipescu test, mesh size, boundary conditions, material coordinate system at the element.

The model is illustrated in Figure 2, 2-D quadratic elements, named CPS4, were used to simulate the specimen deformation under plane stress condition while the clamps were simulated using four rigid contact bodies, two at each side. The specimen can be divided in three parts, at the sides there are the zones held by the clamps and at the center there is the area of measurement, where the displacement field is supposed to be measured with the full-field optical technique. A fixed 0.33 mm mesh size was adopted in each configuration. The reason why only the middle part of the specimen is considered for the measurement is that the two other parts (in the clamps) undergo little deformation. Also, measuring over the whole length will deteriorate the spatial resolution because of the large aspect ratio of the specimen.

The rigid bodies on the left side are fixed while a vertical displacement U_Y^0 is given to the rigid bodies on the right to simulate the shear loading.

A friction coefficient $\mu = 0.05$ is used in the contact properties to prevent sliding in the horizontal direction. The applied force F is obtained as sum of the vertical reactions of the rigid bodies at the right.

Two systems of cartesian coordinates are introduced, the reference global coordinate system $(0, \overrightarrow{X}, \overrightarrow{Y})$, fixed, and the material coordinate system $(0, \overrightarrow{x}, \overrightarrow{y})$ in which the x-axis is aligned with the fibre orientation. The angle α measures the rotation of the material coordinate system with respect to the global one and is the first design variable. The second is the free length of the specimen L, illustrated in Figure 2.

All the other geometric parameters are kept constants, the height H is set equal to 20 mm and the part of the specimen grabbed by the clamps measures 23 mm. The reason for this choice is that the fixture can only accommodate a fixed width whereas it can be used for different free lengths (Pierron, 1994).

It is worth noting that although only two parameters of the test configuration have been taken into consideration, L and α respectively, their variation modifies the stress and strain fields inside the measurement area in a non trivial way. Indeed, the stress state in the unnotched Iosipescu test is a composition of compression, bending and shear as illustrated in Figure 3. Looking at the stress components expressed in the global coordinate system, in the Y-direction the normal stress is mainly compressive and concentrated near the contact zones; in the X-direction the stress state is due to bending and exhibits both tension and compression; shear stresses are also present, as expected from such a shear test. The relationship between the three components strongly depends on the specimen aspect ratio and stiffness which are functions of the chosen design variables.

The thickness of the specimen is set to 3 mm. However, because of

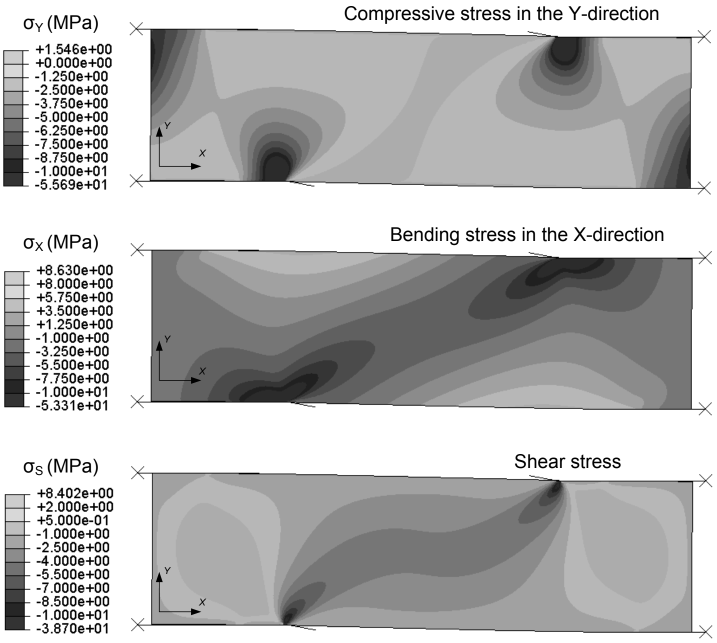

Figure 3: Stress state in the Iosipescu test (global coordinate system): compression stress near the contact zones in the Y-direction, stress due to bending in the X-direction, shear stress. The specimen has a free length $L = 30$ mm and a fibre angle $\alpha = 30°$, the material is glass/epoxy UD and the applied force 100 N.

the plane stress assumption, this value does not influence the identification though in practice, thick specimens are very difficult to load in plane (Pierron, 1998).

3.2. Force and displacement scaling

In an actual measurement, the magnitude of the measured displacement field impacts directly the signal to noise ratio. In general, the scatter of the identified parameters decreases as the maximum displacement (or the applied load) increases. This has been observed, for instance, in some experimental results obtained for similar applications (Xavier et al., 2007).

In order to compare different specimen configurations, which exhibit different stiffness, a normalization procedure is necessary. For example, in Syed-Muhammad et al. (2009), where different test configurations have been studied to identify the bending rigidities of an anisotropic plate, the minimization criterion was normalized with respect to the maximum deflection.

In this work, the normalization was performed during the computation of the displacement field. For each evaluated configuration, the displacement field is the one that corresponds to the maximum force that can be applied to the specimen. The maximum allowable force can be determined using a failure criterion. In practical experiments, the load is limited by the premature fracture of the specimen or by the deviation from linear elastic behaviour.

Many theories are available to predict failure in composites, a good review and a comparison between different approaches can be found in Soden et al. (1998, 2004). The Maximum Stress failure criterion was adopted here for the sake of simplicity. It states that the material is undamaged when the following conditions are fulfilled:

$$S_{-x} \leqslant \sigma_x \leqslant S_{+x}, S_{-y} \leqslant \sigma_y \leqslant S_{+y}, |\tau_s| \leqslant S_s \tag{10}$$

where S_{+x} and S_{+y} are the maximum allowable tensile stresses along and transverse to the fibre directions, respectively, S_{-x} and S_{-y} are the maximum allowable compressive stresses and S_s is the ultimate in-plane shear stress. Obviously, the stress tensor is computed in the material coordinate system.

Although this assumption is quite simplistic, the model is widely used in practice and even more complex theories utilize it to restrict the elastic range where no damage is observed (Zinoviev et al., 1998, 2002). Here it is just used to provide a more physical normalization of the stress and strain levels.

Under the assumption of small displacement and linear elastic behaviour, the stress and strain fields are proportional to the applied force. If F is the force computed by the FEM as the vertical resultant of the imposed fixed displacement U_y^0 on the right part of the fixture, the maximum allowable force, according to the failure criterion, is obtained by scaling the FE reaction force by a factor k, with

$$k = \min\left[\max\left(\frac{\sigma_x^i}{S_{+x}}\right), \max\left(\frac{\sigma_x^i}{S_{-x}}\right), \max\left(\frac{\sigma_y^i}{S_{+y}}\right), \max\left(\frac{\sigma_y^i}{S_{-y}}\right), \max\left(\frac{\tau_s^i}{S_s}\right)\right] \tag{11}$$

and σ_x^i, σ_y^i and τ_s^i the stress components at each i^{th} Gauss point of the numerical model and $\max(\bullet)$ is the maximum over all the Gauss points. In the same way, the displacement field corresponding to the maximum allowable force is then obtained by the same scaling factor k.

	Glass/epoxy UD	Carbon/epoxy UD	Glass/epoxy 0/90°	Carbon/epoxy 0/90°
E_{xx} (GPa)	40	135	25	70
E_{yy} (GPa)	10	10	25	70
G_{xy} (GPa)	4	5	4	5
ν_{xy}	0.3	0.3	0.2	0.1
S_{+x} (MPa)	1000	1500	440	600
S_{-x} (MPa)	-600	-1200	-425	-570
S_{+y} (MPa)	40	50	440	600
S_{-y} (MPa)	-100	-250	-425	-570
S_s (MPa)	40	70	40	90

Table 1: Reference properties for four composite materials. Data from www.performance-composites.com (2010). For the glass/epoxy unidirectional, data from Tsai and Hahn (1980).

Two different composites have been investigated, glass/epoxy and carbon/epoxy, looking at two different fibre configurations, unidirectional (UD) and 0°/90°, for a total of four materials. Typical properties for the materials can be found in various technical or commercial catalogues, the values used in this work are listed in Table 1. The idea here was to explore the effect of anisotropy on the optimal configuration.

3.3. Synthetic images

Analytically, a black and white image can be described as a continuous function $I(\overrightarrow{R})$ of the grey level, where $\overrightarrow{R}$ is the position vector of Section 2.1 defined over a spatial domain that represents the image size. Let us consider $I_r(\overrightarrow{R})$ as the grey level function for the reference image and $I_d(\overrightarrow{R})$ that of the deformed image, distorted according to a given material transformation Φ_M. The two functions can be put in relation using the optical flow conservation:

$$I_d\left(\overrightarrow{R}\right) = I_r\left(\Phi_M^{-1}\left(\overrightarrow{R}\right)\right) \tag{12}$$

In the general case of a displacement field $\overrightarrow{u}$ the transformation function becomes:

$$\Phi_M = \overrightarrow{R} + \overrightarrow{u}\left(\overrightarrow{R}\right) \tag{13}$$

The function $I_r(\overrightarrow{R})$ represents, in terms of grey levels, the pattern printed in the specimen surface before deformation starts. For instance, using digital image correlation, the pattern will be a series of speckles with random size. An example of speckle simulation can be found in Orteu et al. (2006). Working with the grid method, the reference image is an equispaced grid which can be described by the following analytical function:

$$I_r\left(\overrightarrow{R}\right) = I_0\left\{1+\gamma\left[\cos\left(\tfrac{2\pi X}{p}\right)+\cos\left(\tfrac{2\pi Y}{p}\right)\right.\right.$$
$$\left.\left.-\left|\cos\left(\tfrac{2\pi X}{p}\right)-\cos\left(\tfrac{2\pi Y}{p}\right)\right|\right]\right\} \quad (14)$$

where I_0 and γ are the quantities defined in Eq. 1 and $\overrightarrow{R} = (X, Y)$ is expressed in the global coordinate system, $|\bullet|$ is the absolute value. The analytical function for the deformed image is obtained using Eq. 12, Φ_M is computed from Eq. 13 using the displacement from the FE model, scaled according to the normalization proposed in Section 3.2.

At this point, two synthetic images are generated digitizing the image functions $I_r(\overrightarrow{R})$ and $I_d(\overrightarrow{R})$. The intent is to reproduce the acquisition process of a digital camera. In a digital camera, an image is projected through a lens onto the photoactive region, which is usually a matrix of CCD sensors. Every pixel of the recorded image corresponds to a CCD sensor of the camera. A CCD sensor is a device able to accumulate an electric charge proportional to the light intensity.

Let us consider a pixel M and the area A_M which represents the portion of the grid imaged by that pixel. The digital value stored in M is an integer proportional to the average light intensity inside the area A_M. The area A_M represents the sensitive part of the pixel and could be varied to simulate different fill factors. In the present case, the light intensity is represented by an analytical function $I(\overrightarrow{R})$, so the digital recorded value $P(M)$ can be computed as follows:

$$P(M) = \left\lfloor \frac{1}{A_M}\int_{A_M} I\left(\overrightarrow{R}\right) dS \right\rceil \quad (15)$$

where $\lfloor\bullet\rceil$ is the nearest integer to the value computed inside.

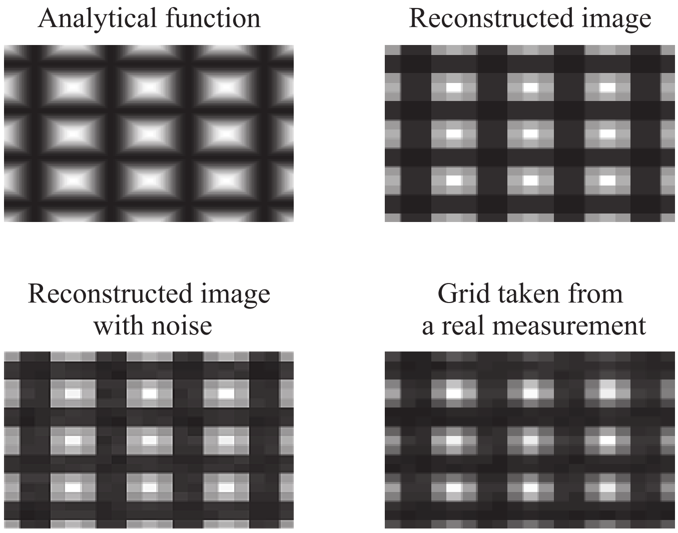

Analytical function

Reconstructed image

Reconstructed image with noise

Grid taken from a real measurement

Figure 4: Generation of synthetic images: starting from the analytical function (Eq. 14) a synthetic image is generated using pixel supersampling and noise is added to the grey level. In the final plot a real grid coming from experiments is shown as a comparison.

The integral in Eq. 15 is numerically computed using pixel supersampling. The function $I(\overrightarrow{R})$ is evaluated at N_p points inside the pixel area A_M and $P(M)$ is computed as an average value:

$$P(M) = \left\lfloor \frac{1}{N_p} \sum_{i=1}^{N_p} I\left(\overrightarrow{R}_i\right) \right\rfloor \tag{16}$$

The generation process of a synthetic image of a grid starting from the analytical function is illustrated in Figure 4, a comparison with a grid taken from an actual measurement is also shown.

The approximation due to the numerical integration and the quantization which occurs at the pixel level influences the phase detection and consequently the measurement precision. To have an idea of such effect a simple test is conducted, two synthetic images are created in order to reproduce a small uniform stretch in the X-direction equal to $5 \cdot 10^{-4}$, then the grid method is used to extract the displacement and compute the strain. The image size is 500×200 pixels and the grid pitch is 5 pixel. Two different dynamic ranges have been considered, 8-bit (256 grey levels) and 12-bit (4096 grey levels) respectively, furthermore three different distributions of the resampling points inside the pixels have been evaluated, the results are illustrated in Figure 5. The obtained strain maps are not constant and a variation is observed from the reference value of $5 \cdot 10^{-4}$. Using an 8-bit dynamic range, the error has a high frequency and it is not influenced by the resampling points, it is mainly due to the quantization error. Using a 12-bit dynamic range, the quantization error is reduced but the WDTF algorithm is disturbed by the high spatial frequencies due to the horizontal lines of the grid. The effect is influenced by the number of resampling points and it disappears if only vertical lines are used to compute the displacement in the horizontal direction instead of a grid.

The synthetic images used in this work simulate the acquisition of a CCD camera with a resolution of 1360×1024 pixels and a grey level range of 12 bit. A matrix of 5×5 sampling points was used to compute the grey level value at each pixel. In this case the errors coming from the digitization are of much lower amplitude than the errors due to the noise.

The noise is simulated by adding a standard Gaussian white noise to the grey level value of each pixel. The mean of the introduced noise is zero, the standard deviation can be varied to simulate different noise levels in the measurements.

The amount of noise in actual measurements depends on several factors (camera, lighting...) and varies largely for different experimental set-ups. It can be measured by recording two pictures of the same reference image

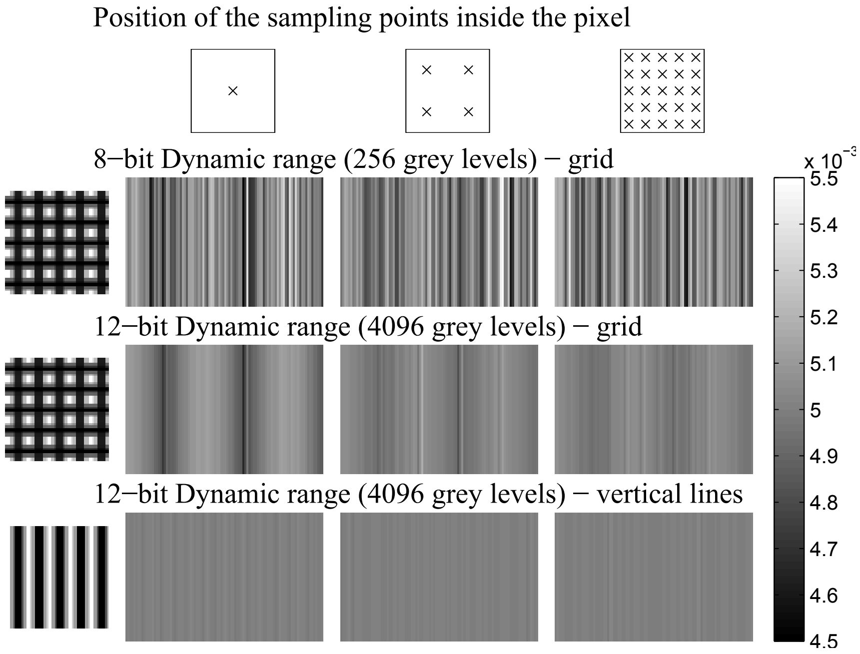

Figure 5: Strain fields obtained from synthetic images which reproduce an uniform stretch equal to $5 \cdot 10^{-4}$. The image size is 500 × 200 pixel and the grid pitch is 5 pixels. Two dynamic ranges are evaluated, 8-bit and 12-bit, and different sampling points are chosen. No noise is introduced, the observed oscillations are caused by the quantization error and the high spatial frequencies of the square grid which disturb the phase detection.

and calculating the corresponding displacement which should be zero in all pixels, if no noise was present. To quantify the noise level, the standard deviation of this "displacement" can be taken (Surrel, 1999; Chalal et al., 2006).

Here a simple test was performed just to estimate a reasonable noise level, in terms of grey levels, to input in the simulation routine. Two pictures of the same reference image were recorded and the noise level was computed as the standard deviation of the difference of the grey levels at each pixel, divided by $\sqrt{2}$ to get the standard deviation of the noise in a single image. Using a 12-bit camera, which has 4096 grey levels, the obtained standard deviation in different tests ranged from 20 to 25 grey levels, $0.5 \div 0.6\%$ of the dynamic range. It would correspond to 1 to 2 grey levels for an 8-bit camera. This value can largely change according to the experimental conditions but the test gives an idea of the order of magnitude.

3.4. Number of measurement points

In full-field optical techniques, displacements are measured at a certain number of points over the surface. With the grid method it is possible to have an independent measurement for each line of the grid. The number of points influences the spatial resolution of the measurement, that is the minimum distance between two independent measurement points. Clearly, a higher spatial resolution will also produce a better identification of the constitutive parameters. Nevertheless, it should be pointed out that a converged FE model has usually at least one order of magnitude less elements than pixels on a standard CCD chip. Therefore, increasing the spatial resolution is mainly necessary for noise filtering purposes.

The number of available measurement points depends also on the shape of the framed area. As explained in Figure 6, the window of the digital camera is fixed, therefore, when a surface is framed, there are some pixels that are not involved in the measurement process, unless the specimen area has the exact aspect ratio of the CCD chip.

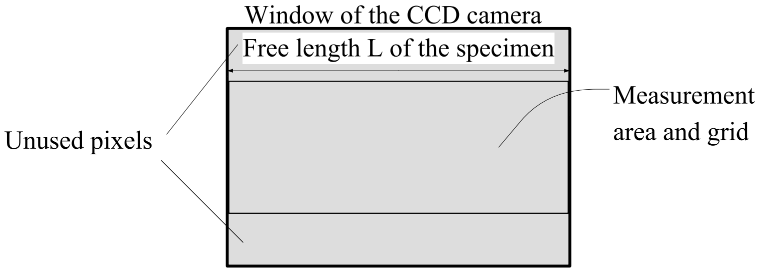

Figure 6: Full-field measurement: the number of pixels that can be really used during the measurement depends on the aspect ratio of the CCD chip and the aspect ratio of the specimen area to be framed.

In other words, this means that it is not convenient to use specimens with too large aspect ratios, because it will decrease the spatial resolution of the measurement. It is important to introduce this aspect to compare the effectiveness of different specimen configurations. This was the main limitation of the approach proposed in Pierron et al. (2007) where only the sensitivity to noise was used in the cost function. In that case it was noticed that the optimization is not very sensitive to the variation of the free length of the specimen. In fact, specimens with a very long or very short free length can still exhibit a low sensitivity to noise. In a real experiment, however, such kind of specimens will lead to a poor identification because their aspect ratio is far from the aspect ratio of the CCD chip.

In order to take this effect into account, a procedure has been developed which finds the configuration that maximizes the number of measurement points, for each specimen geometry. First the orientation of the camera is set to maximize the framed area. The camera can be used in a vertical or horizontal position. Once the best orientation has been defined, the grid pitch is chosen in order to have a period every five pixels in the undeformed image.

As explained in Section 3.1, the height of the specimen is kept constant while the free length is varied. As the length decreases, the measurement area is reduced too. A magnification has to be performed to frame the whole area with the camera. As consequence, the pitch of the grid has to be reduced in order to keep a period each five pixels of the image. In actual applications, the grid size can not be reduced under a certain level, see Section 2.1. Here the minimum allowable grid pitch is assumed to be 100 μm (Piro and Grédiac, 2004), below this limit the magnification is kept constant in order to preserve a period every five pixels and the camera does not frame the whole measurement area.

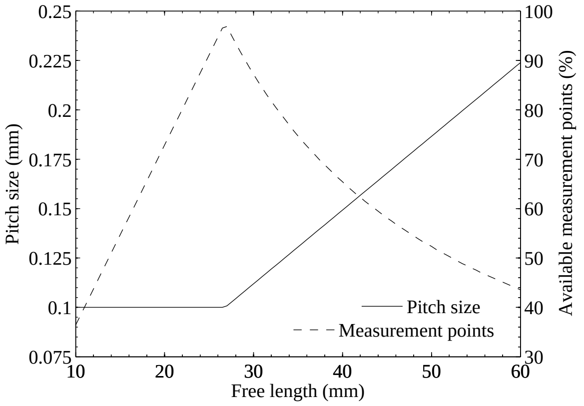

Figure 7: Grid pitch size and percentage of the available measurement points as a function of the gauge length L. The aspect ratio of the camera is fixed and equal to 1.328. The camera magnification is adjusted in order to have a period of the grid every 5 pixels.

The results obtained with the proposed procedure are summarized in

Figure 7. The measurement points and the grid pitch size are plotted as a function of the free length L. The measurement points are given as a percentage of the maximum number of available measurement points. The maximum number of available measurement points depends on the type of camera. Using a CCD camera with a resolution of 1360×1024 pixels, if all the pixels are involved in the measurement and a measurement point can be obtained every five pixels, theoretically it is possible to have 272×204 measurement points.

The maximum number of measurement points in the simulated experiment is reached for $L \simeq 27$ mm. In this case the aspect ratio of the measurement area approaches the aspect ratio of the CCD chip. Here, it also corresponds to the minimum of the grid pitch.

4. Results and discussions

Simulated experiments were then employed to study in detail the unnotched Iosipescu test. The design variables that lead to the best identification were evaluated using a cost function. Different materials have been taken into consideration to study the effect of anisotropy. Besides, other practical aspects have been analyzed: the effect of smoothing and the influence of missing data.

4.1. Cost function

A cost function has to be defined to compare different configurations and find out which one provides the best identification of the material parameters. For a given set of design variables, the cost function represents the error in the identification averaged over N_e simulated experiments, it writes:

$$\Phi(L,\alpha) = \frac{1}{N_e}\sum_{k=1}^{N_e}\sqrt{\sum_{ij} w_{ij}\left(1-\frac{Q_{ij}^{(k)}}{Q_{ij}^{(0)}}\right)^2} \quad \text{with} \quad ij = [xx, yy, xy, ss] \quad (17)$$

$Q_{ij}^{(0)}$ are the reference parameters to be identified, $Q_{ij}^{(k)}$ are the parameters identified at the k^{th} simulated test and w_{ij} is a weighting parameter that can be varied to give more or less importance to a particular stiffness component during the optimization process.

A Matlab routine has been implemented to compute the cost function automatically and it is summarized in the flow chart in Figure 8. The input data are the material properties, the design variables, the spatial resolution and dynamic range of the CCD camera and the amount of noise. The program generates automatically the FE model, computes the maximum allowable load for the current configuration and the corresponding displacement field in the measurement area. According to the CCD camera characteristics two synthetic images are generated, for the reference and the deformed configuration, respectively. The noise is added to the images and subsequently they are processed using the grid method in order to extract the displacement and the strain fields. If the introduced level of noise is particularly high, it is possible to utilize smoothing functions to compute the strain. The constitutive parameters are identified using the optimized VFM (see Section 2.2) and the cost function Φ is evaluated.

4.2. Parameter identification for a glass/epoxy unidirectional composite

A first analysis was conducted on a glass/epoxy unidirectional composite since experimental data are available for this material (Pierron et al., 2007). The free length L was varied from 10 to 60 mm with a step of 2 mm while

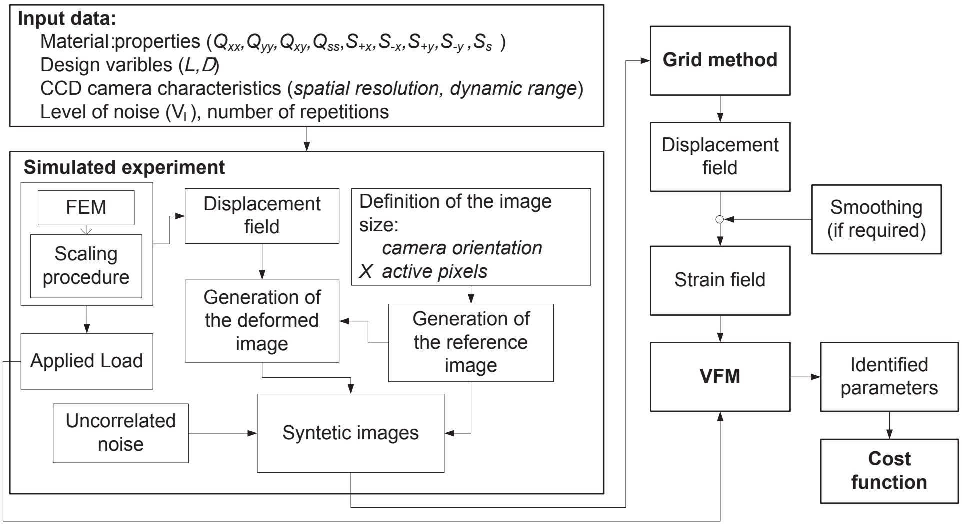

Figure 8: Flow chart of the Matlab routine used to compute the cost function.

the fibre angle α was varied from 0° to 90° with a step of 5°. The standard deviation of the added noise is equal to 30 grey levels, which corresponds to 0.7% of the total dynamic range. The strain field was computed using direct differentiation and no smoothing. For each configuration, 30 simulated experiments were run.

At the end of the simulation process, the identified parameters are used to evaluate the cost function by Eq. 17. The cost function can be plotted as a contour map in the plane of the design variables L and α, Figure 9. In this map, the cost function is computed using the same weight for each parameter, $w_{ij} = 0.25$, so that it represents an average of the identification error. The function itself is somewhat noisy because of the random nature of the processed information and the limited number of trials (30). Therefore a Gaussian filter was applied, using a standard convolution method, in order to get a smoother function that can be minimized more easily (Haddad and Akansu, 1991). The convolution matrix involves 5×5 measurement points and it is computed using a Gaussian function with a 0.75 standard deviation and 1 as normalized distance between two measurement points. Another option could have been to increase the number of simulated experiments, but it would have increased the computational time too much .

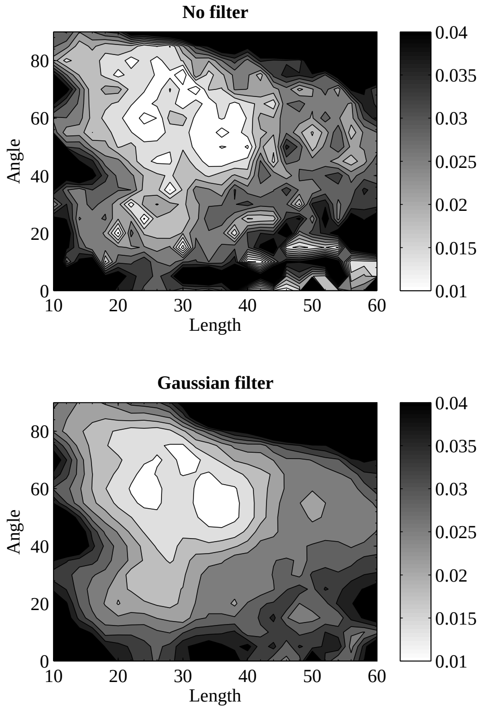
No filter

Gaussian filter

Figure 9: Cost function evaluated for glass/epoxy UD. Standard deviation of noise: 30 grey levels, 30 repetitions for each configuration. In the second plot a Gaussian filter is applied to have a smoother result.

The best identification is obtained when the free length is between 20 and 35 mm and the angle between 50° and 75°. The cost function for each stiffness can be studied separately by respectively setting $w_{ij} = 1$ for one value of ij and $w_{ij} = 0$ for the others, Figure 10.

Looking at the scale of the contours parameter Q_{ss} is the easiest to identify and parameter Q_{xy} is the most difficult as expected from Pierron et al. (2007). The identification of parameters Q_{xx} and Q_{yy} principally depends on the fibre angle orientation, this is not surprising since the two parameters represent respectively the stiffness on the x and y directions, therefore the best situation is when the fibers are aligned with the main direction of the bending stress, $0°$ for Q_{xx} and $90°$ for Q_{yy}. The identification of Q_{ss} is better when the fibre angle is around $0°$ or $90°$ where the shear stress is predominant in the material coordinate system. For parameter Q_{xy}, the best situation occurs for an angle $\alpha \simeq 60^o$ and a length $L \simeq 20$ to 35 mm. All these considerations are in agreement with what was already found in previous studies using different approaches (Pierron et al., 2007; Xavier et al., 2005).

The cost function represents an average of the identification error and takes into account both the bias and the standard deviation. It could be interesting to evaluate the error distribution for single configurations. In Figure 11 a histogram is plotted with the identification of the single parameter Q_{xx} for two specimen configurations, $L = 36mm$, $\alpha = 50°$ and $L = 16mm$, $\alpha = 15°$ respectively. In Figure 11(a) simulated images have been used to obtain the strain field. A level of noise of 30 grey levels and 100 test repetitions have been used. The same test is then repeated without simulating the measurement process but simply introducing a similar amount of noise in the strain fields computed by FEM, Figure 11(b), in this case the only source of error is the noise itself. For the first configuration the results are very similar, but in the second configuration which represents a non optimal solution (see the cost function plot in Figure 9) a bias is observed when synthetic images are used to compute the strain fields and not

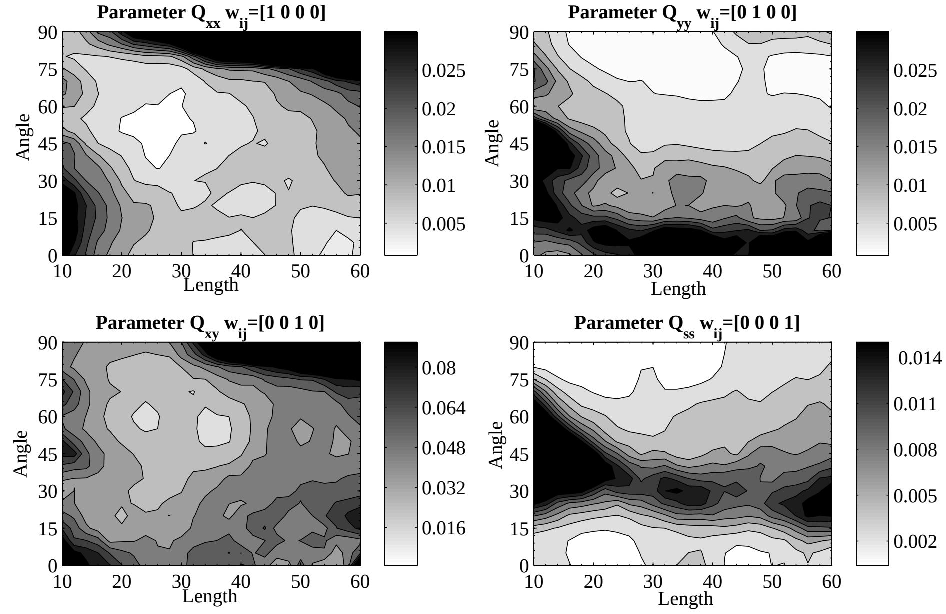

Figure 10: Cost function evaluated separately for each parameter of the constitutive equation, glass/epoxy UD. Standard deviation of noise: 30 grey levels, 30 repetitions for each configuration.

when the FEM strain data are used. Probably the bias is due to the lower spatial resolution obtained in the second configuration where a non optimal aspect ratio is used, for this reason the measurement technique is not able to correctly measure the strain in the zones of the specimen with a high strain gradient. To be sure that the error is not related to the strain computation, another test has been performed and illustrated in Figure 11(c). Here the noise was applied to the displacement field obtained from the FEM and then the same strain computation procedure adopted as in the first case was used to compute the strain field. No bias is observed in this case either, confirming that the bias comes from spatial resolution issues related to the full-field measurement itself.

The analysis highlights that errors are hidden in the acquisition process itself and they end up influencing in some way the identification. The advantage (and novelty) of the proposed approach is that all these errors are embedded in the procedure and are implicitly introduced in the evaluation of the cost function.

The importance of the number of measurement points in the identification can be proved by simulating a camera with a different CCD chip aspect ratio. A hypothetical camera with a resolution of 1360×512 pixels was used. As illustrated in Figure 12, the shape of the cost function is now totally different and it can be directly related to the number of measurement points which is plotted below the cost function maps as a function of the specimen length L. The lowest values of the cost function are obtained where the number of measurement points is maximum. Besides in the second case the average value of the cost function is two times larger as the size of the CCD chip is decreased by a half. This clearly indicates the effect of the spatial resolution that the present procedure simulates efficiently.

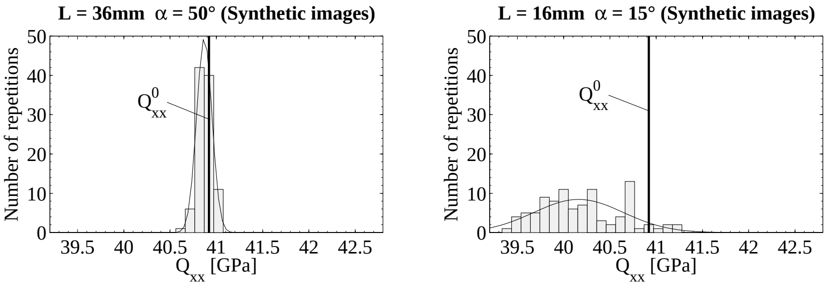
L = 36mm α = 50° (Synthetic images)

L = 16mm α = 15° (Synthetic images)

(a) Simulation of synthetic images

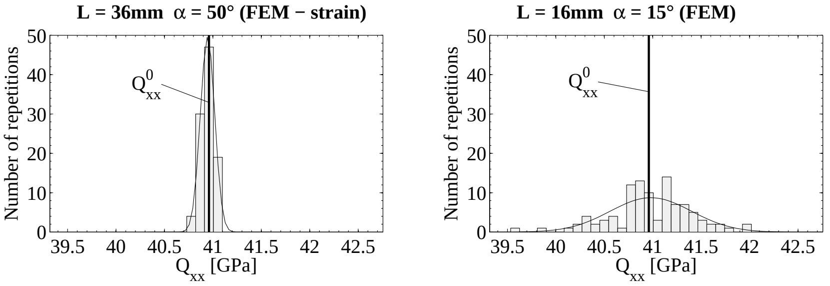
L = 36mm α = 50° (FEM − strain)

L = 16mm α = 15° (FEM)

(b) Noised strain field

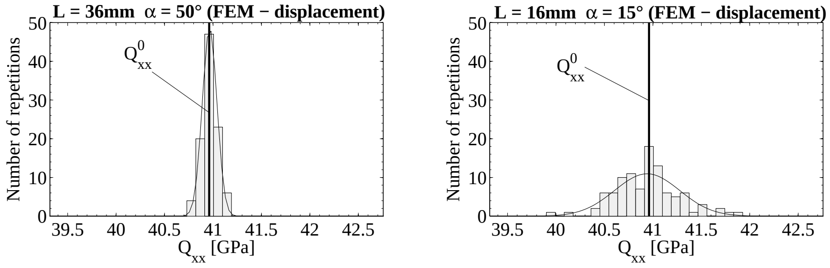
L = 36mm α = 50° (FEM − displacement)

L = 16mm α = 15° (FEM − displacement)

(c) Noised displacement field

Figure 11: Histograms of the identified parameter Q_{xx} for two specimen configuration, $L = 36, \alpha = 50^\circ$ and $L = 16, \alpha = 15^\circ$ respectively. A level of noise equal to 30 grey levels and 100 repetitions have been used. Subsequently, the same tests are reproduced without simulating the images, but simply introducing a similar amount of noise directly on the strain field or on the displacement field computed by the FEM.

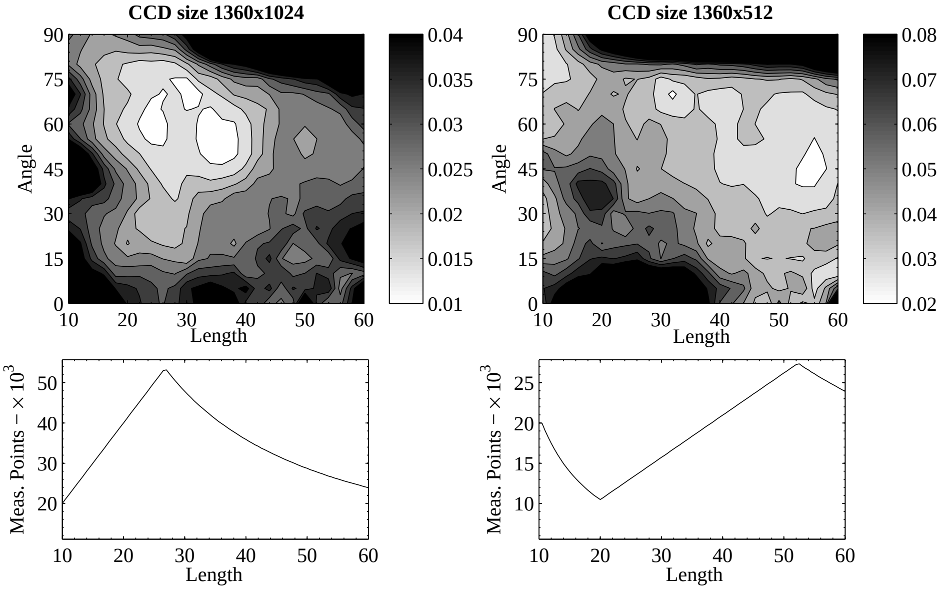

Figure 12: Effect of the number of measurement points. The size of the CCD chip changes the shape of the cost function. The lowest values are observed where the number of measurement points is maximum.

It is beyond the purpose of this paper to give an experimental validation of the proposed technique, an extended experimental study will be conducted in the future. Nevertheless a first check can be made using the results obtained by Pierron et al. (2007) using the unnotched Iosipescu test on the same material, glass/epoxy UD.

In this study, the unnotched Iosipescu test was performed on two types of specimen, the first with $L = 30$ mm and $\alpha = 0^o$ (5 repetitions) and the second with $L = 40$ mm and $\alpha = 25^o$ (6 repetitions). The cost function Φ can be computed from the experimental data using Eq. 17 and compared with the cost function obtained using simulated experiments with the same geometry and fibre orientation. The reference values $Q_{ij}^{(0)}$ for the experiments are taken as the average of the values measured at each test.

Actually, it is still not possible to compare directly the cost functions because the level of noise in the experiments is not known, therefore a normalized cost function is introduced. First the cost function was evaluated separately for each parameters as seen before, then these values were normalized by the average error which is obtained with $w_{ij} = 0.25$. The same procedure was repeated for both the experimental and the simulated data. The comparison is illustrated in the bar plot of Figure 13.

A mismatch is normal because of the low number of repetitions available in the experimental tests. However the simulated procedure is able to reproduce qualitatively the trend observed in the experiments. Parameter Q_{xx} is identified with good accuracy in both configurations. The identification of Q_{yy} however is much better in the 25° configuration. Q_{ss} has a good identification in both cases but the 0° configuration gives the best outcome. About Q_{xy}, which is the most difficult parameter to identify, more scatter is expected, nevertheless the experiments show a better identification in the

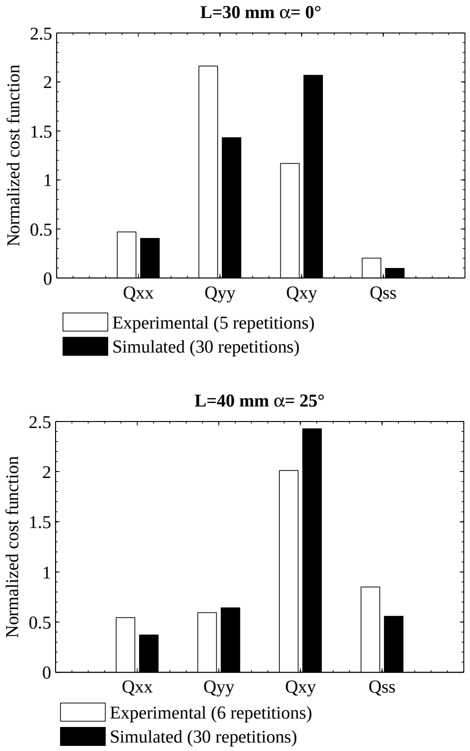

Figure 13: Comparison between simulated and actual experiments from Pierron et al. (2007). The cost function was normalized dividing by the average error, two configurations were evaluated.

0° configuration and the same trend is obtained using the simulated data.

This is only a first analysis, more experimental tests are needed. However the developed procedure seems to be reliable in comparing different configurations.

4.3. Sensitivity to scaling

The scaling procedure introduced in Section 3.2 influences the cost function. The adopted failure criterion is quite simplistic and the limit stresses listed in Table 1 are generic values for a class of material. In order to have reliable results in the optimization, it is important to verify that the cost function is not strongly dependent on these parameters.

A sensitivity study was conducted on glass/epoxy UD. According to the Maximum Stress criterion, for each configuration, only one of the five limit stresses will be involved in the scaling procedure, see Eq. 11. The first plot of Figure 14 shows the parameters driving the scaling for glass/epoxy UD. This scaling is mainly driven by the maximum stresses in the transverse direction (S_{-y} and S_{+y}). In order to assess the sensitivity of the proposed procedure to the scaling parameters, the cost function was evaluated using the same test conditions but increasing the failure stresses S_{-y} and S_{-y} by 50%.

The comparison of the cost functions obtained with the increased values and the reference one is also illustrated in Figure 14. The plots look similar, no remarkable changes are produced by increasing the limit stress. This check suggests that the procedure will return similar results if the material properties are chosen within a reasonably wide range.

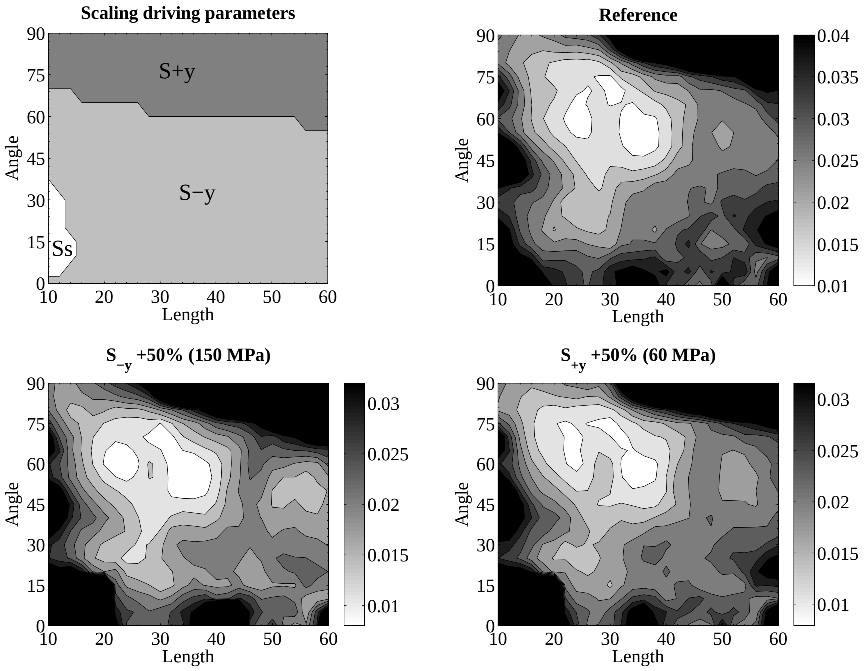

Figure 14: Sensitivity of the cost function to scaling. In the first plot the parameters driving the scaling for the glass/epoxy UD are illustrated. Then the cost function was evaluated increasing the maximum stresses in the transverse direction by 50% ($S_{-y} =$ 150 MPa and $S_{+y} = 60$ MPa).

4.4. Effect of anisotropy

The cost function described previously can be used to optimize the test configuration. Indeed the best set of design variables can be considered as the one that minimizes the cost function. The purpose of this section is to study how this choice is influenced by the material anisotropy. Four different composite materials were analyzed, the mechanical properties have already been reported in Table 1.

The cost function was evaluated using the same weight ($w_{ij} = 0.25$) for the four parameters. The test conditions are the same adopted for the glass/epoxy UD, 30 repetitions per configuration, standard deviation of the noise added to the images equal to 30 grey levels. The strain field was computed by direct differentiation from the displacement data.

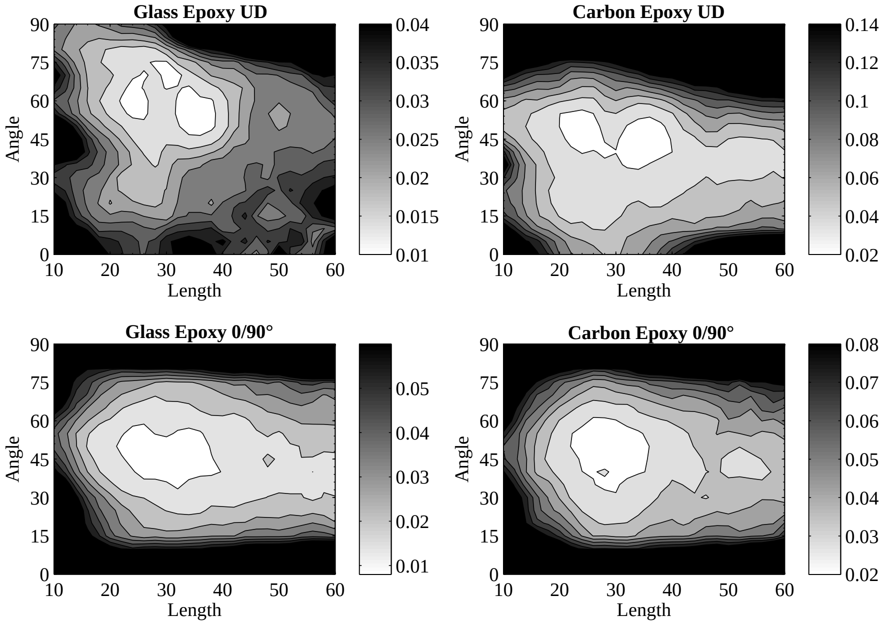

Figure 15: Cost function evaluated for four materials as a function of the design variables. Standard deviation of noise: 30 grey levels, 30 repetitions for each configuration.

	L(mm)	α (degree)	Φ
Glass/epoxy UD	24.3	62.4	0.0122
	37.2	52.9	0.0125
Carbon/epoxy UD	23.0	50.8	0.0258
	33.6	50.3	0.0289
Glass/epoxy 0°/90°	31.2	48.6	0.0122
Carbon/epoxy 0°/90°	31.3	43.6	0.0233

Table 2: Values of the design variables that minimize the cost function

The cost function for the different materials is plotted in Figure 15. For each material, the best set of design variables is the one corresponding to the lowest value of the cost function. Since the function has been evaluated discretely ($L = 10 : 2 : 60$, $\alpha = 0 : 5 : 90$), the minimum point was obtained using a polynomial interpolation in the neighbourhood of the discrete minimum (Vanderplaats, 1984). The optimized design variables for the four materials are reported in Table 2.

For the UD materials two local minima can be found where the cost function is almost equal. In the 0°/90° configuration the function Φ should be theoretically symmetrical with respect to 45°, but a small deviation from this condition is observed because of the random noise.

As a general consideration, although the material properties are rather different, the optimized solutions do not differ too much. A free gauge length L = 30 to 35 mm gives good results in all cases. This fact is due to the better spatial resolution gained thanks to the larger number of measurement points available in this case. As rule of thumb, it can be concluded that a good test will be such that the gauge area follows the aspect ratio of the CCD camera.

As for the fibre orientation, the optimum value for the 0°/90° configurations is $\alpha = 45^o$, while it is slightly higher ($\alpha = 50$ to 60^o) for the UD configurations.

However, the anisotropy influences the quality of the identification. Indeed, looking at the scale of the contour maps, it follows that the best identification is obtained for the glass/epoxy composites that have a less pronounced anisotropy than the carbon/epoxy composites. In particular the most anisotropic material, the carbon UD, shows the worst identification in terms of cost function.

The different levels of anisotropy also influence the shape of the cost function in the two unidirectional composites. The identification of the carbon/epoxy UD becomes particularly difficult when the fibre angle orientation goes over 60°. This problem is less evident in the glass/epoxy UD, especially when the free length is less than 30 mm.

4.5. Effect of smoothing

The strain field is not directly obtained from the measurements but is computed as a differentiation of the displacement field. A point to point differentiation tends to magnify the effect of noise, for this reason smoothing functions are commonly introduced to derive the strain field from the displacement field. Using a simulated experiment the level of noise can be controlled and the influence of the smoothing in the identification can be studied in detail.

As an example, Figure 16 shows the component ε_Y of the strain tensor computed with different noise levels. The simulated specimen has a free length of 30 mm and a fibre orientation of 50°. On the left the strain is obtained through direct differentiation, on the right using a smoothing function, namely second order polynomial diffuse approximation (PDA), with a span radius of 12 pixels (Avril et al., 2010, 2008b). Three levels of noise were considered: 10 grey levels (0.2% of the dynamic range), 30 grey levels (0.7% of the dynamic range) and 150 grey levels (3.7% of the dynamic range). The strain field computed with direct differentiation appears blurred while the PDA supplies a fine strain reconstruction.

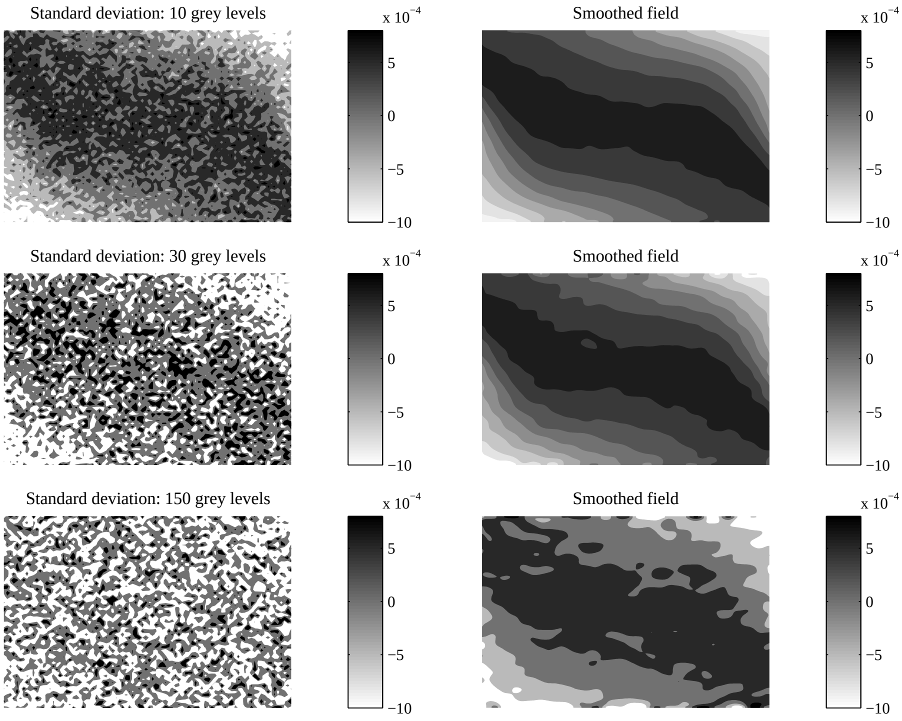
Standard deviation: 10 grey levels

Smoothed field

Standard deviation: 30 grey levels

Smoothed field

Standard deviation: 150 grey levels

Smoothed field

Figure 16: Computation of the strain field from the measured displacement field: comparison between the results obtained with and without smoothing, at different noise levels. Component ε_Y of the strain tensor. Smoothing performed with polynomial diffuse approximation with a span radius of 12 pixels (Avril et al., 2008b). Material: glass/epoxy UD.

The effect of smoothing on the parameter identification is less straightforward. A test was conducted on the same specimen configuration, L=30 mm and $\alpha = 50°$, at different levels of noise. For each noise level, the strain was computed using direct differentiation, PDA with a span radius of 12 pixels and a global polynomial fitting with a 7^{th} degree polynomial function. The cost function was evaluated from the reconstructed strain data and plotted as function of the noise level, Figure 17.

The graph shows that smoothing improves the identification only beyond a certain value of noise. In the studied configuration, this noise threshold is around 15 grey level for the PDA and 40 grey levels for the polynomial fitting. After 60 grey levels the polynomial fitting returns the best identification. This behaviour can be seen as surprising, since looking at the strain maps of Figure 16, even with a noise standard deviation of 10 grey levels, the strain field computed with smoothing looks qualitatively much better compared to the one computed with direct differentiation.

An explanation can be given on the basis of the VFM theory, see Eq. 8. To identify the parameters, the measured strain components are multiplied by the virtual strain components, which can be viewed as weighting functions, and integrated over the surface. The integration gives a first filtering of the strain data. Furthermore, using smoothing, the perturbation error due to the noise decreases but the approximation error increases because the smoothing acts as a low-pass filter. The balance between these two reconstruction errors makes the smoothing convenient only after a certain noise threshold. The polynomial fitting, that provides strong smoothing of the data, works well for high levels of noise but the reconstruction error is larger for small noise level (bias).

This aspect has been studied more deeply using PDA. In fact, the smoothing capability of PDA can be changed by varying the span radius R of the

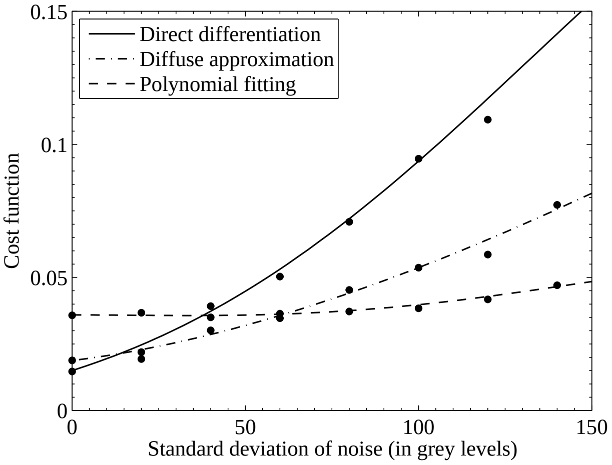

Figure 17: Effect of smoothing in the identification. The cost function was evaluated as function of the noise level. Two smoothing functions are compared: PDA with a span radius of 12 pixels and a polynomial fitting with a 7^{th} degree polynomial function. Material: glass/epoxy UD.

averaging function. The larger R the smoother the reconstructed strains, since more points are used in the averaging. A series of tests were performed keeping constant the noise level and varying the span radius of PDA. The results are illustrated in Figure 18 in terms of cost function and reconstruction error. The reconstruction error is defined as the quadratic distance between the reconstructed strain field and the exact one (Avril et al., 2008b):

$$e_{\varepsilon} = \left\langle \sqrt{\left(\varepsilon_x^{rec} - \varepsilon_x^{ex}\right)^2 + 2\left(\varepsilon_s^{rec} - \varepsilon_s^{ex}\right)^2 + \left(\varepsilon_y^{rec} - \varepsilon_y^{ex}\right)^2} \right\rangle_{\Omega_m} \tag{18}$$

where $\langle \bullet \rangle_{\Omega_m}$ is the average of the data over region Ω_m, the whole measurement area.

Looking at the cost function, the span radius influences the identifications only when a large noise is introduced in the measurements. The same trend is not observed in the reconstruction error, in this case an increasing R gives a better result also for low levels of noise. It can be concluded that the reconstruction error measured on the whole area is not a reliable output to evaluate the quality of the identification. Actually, the reconstruction error gives the average error over the whole surface of the specimen. However, some parts of this surface, for instance where the strains are low, do not influence the identification and should not be taken into consideration. The proposed cost function seems to be a more relevant tool to decide which type of smoothing is convenient to use in a real measurement. Of course, all these considerations are valid under the hypothesis of a Standard Gaussian distribution of noise but it can be expected that trends will be the same for other noise distributions.

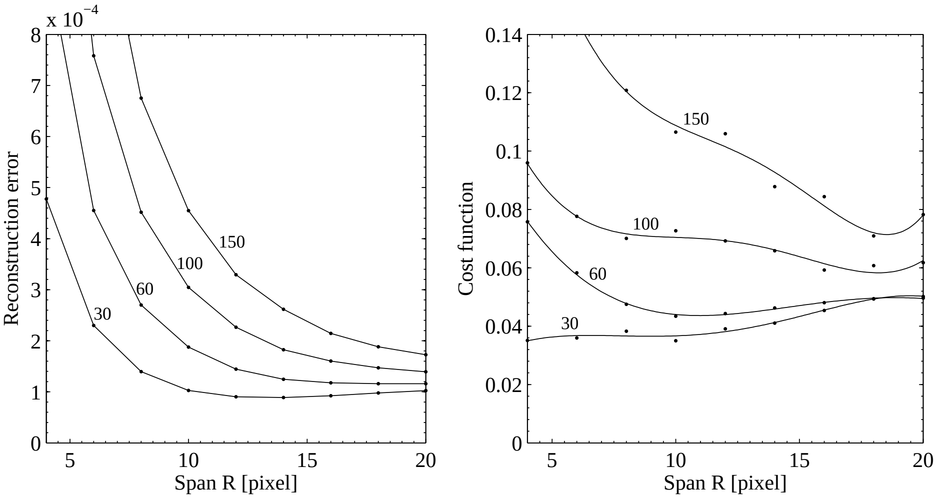

Figure 18: Effect of the span R on the strain reconstruction and on the identification using the VFM, at different noise levels. Material: glass/epoxy UD.

Another issue is how the smoothing function influences the choice of the design variables, or, in other words, if the optimized specimen configuration obtained for a given material in section 4.4 is still valid when a smoothing function is applied.

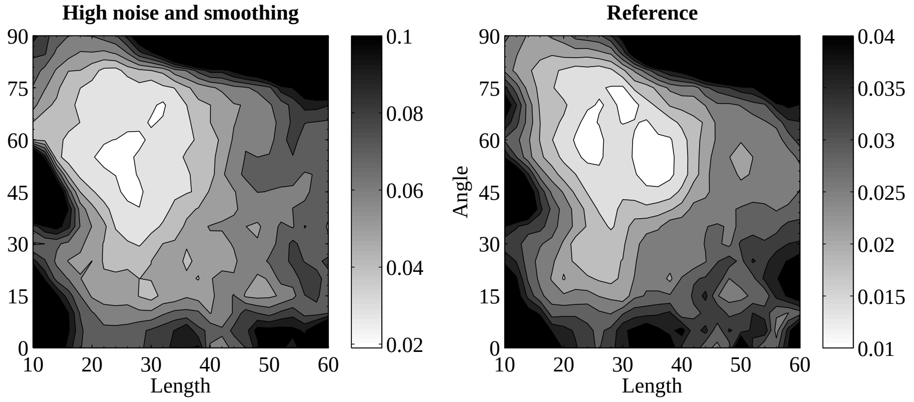

Figure 19: Cost function obtained introducing a high level of noise in the synthetic images (standard deviation: 150 grey levels) and using the PDA algorithm, with a radius of 20 pixels, to compute the strain field. 10 repetitions for each test. Material glass/epoxy UD. The reference plot corresponds to the cost function of Figure 9.

The same procedure used to determine the optimal design variables on glass/epoxy UD was repeated using an increased level of noise (standard deviation: 150 grey levels) and PDA to compute the strains, with a large span radius of 20 pixel. Only 10 repetitions were used at each configuration because of the long time required by the PDA algorithm. The results are presented in Figure 19, the reference plot is the cost function evaluated for the same material in Figure 9. Qualitatively, the two cost functions look similar. In this case a minimum was found for $L = 29.8$ mm and $\alpha = 57.5^o$, not too far from the values obtained previously and listed in Table 2. Clearly, looking at the contour scales in the two cases, the average identification error is higher when more noise is introduced. In order to prove the effectiveness of the PDA in reconstructing the strain field it can be highlighted that, although the standard deviation of the noise was increased five times, from 30 to 150 grey levels, the average error in the identification increases only by a factor of around two.

On the basis of these results, it seems reasonable to conclude that an optimized configuration found using a low level of noise and no smoothing will be effective also when a high level of noise is encountered. From a practical point of view, the possibility of excluding the smoothing process in the optimization algorithm, where the cost functions have to be evaluated many times, allows to save a lot of computational time.

4.6. Influence of missing data

During a real test it is always difficult to measure the displacement at the free edges of the specimen and some data are commonly lost. This is particularly true for digital image correlation but also to a lesser extent for the grid method where one line at least is lost (5 pixels) because of the WDFT algorithm used to extract the phase (Surrel, 1996). The VFM requires the measurement of the displacement field up to the free edges of the specimen therefore, when data are missing on the top or on the bottom, an error is inevitably introduced in the identification. In order to assess the magnitude of this error, a test was conducted using a specimen with $L = 30$ mm and $\alpha = 50°$ for which rows of data from the top and the bottom of the specimen have been removed.

As illustrated in Figure 20, the identification is rather dependent on missing data. For instance, if 25 pixels are removed at the two edges of the measurement area the error in the identification is almost double. In this specimen configuration, 25 pixels correspond to around 1 mm in metric units. This strong dependence is probably due to the bending load in the

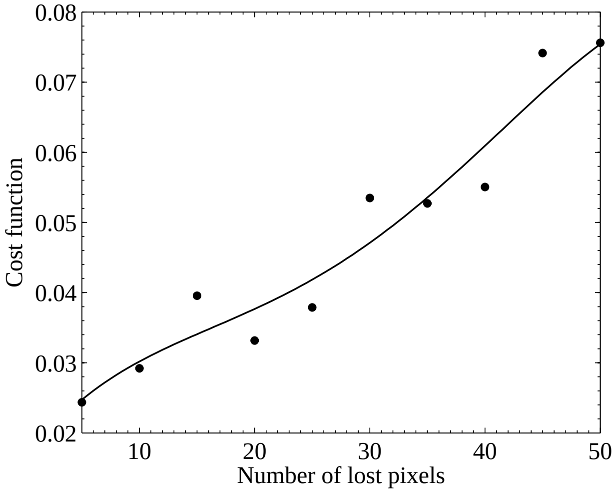

Figure 20: Identification error as a function of the pixels which are removed from the edges of the specimen

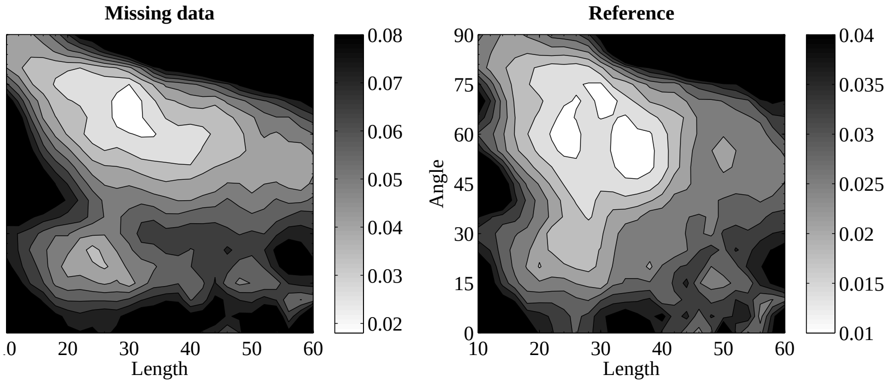

Figure 21: Cost function with five rows of measurement points missing at each edge, material: glass/epoxy UD, standard deviation of noise: 30 grey levels. The reference plot corresponds to the cost function of Figure 9.

Iosipescu test which has maximum bending stress and strain at the edges of the specimen.

Figure 21 shows the cost function for glass/epoxy UD when five rows of points are removed from the top and the bottom of the measurement area. In a similar way as to what was observed for the smoothing, the missing data slightly influence the shape of the cost function with respect to the design variables but principally increase the mean value of the error. The average error is almost double compared to the reference plot, for the same material and the same amount of noise. Comparing the two contour plots, it can also be noticed that the missing data influence more the identification when the fibre angle varies between 10° and 35°.

In this case we considered only missing data at the edges of the specimen. In actual experiments imperfections of the grid transfer onto the sample surface could produces missing data also inside the measurement area. Although such effect has not been taken into account in the present study, it could be simulated using the same proposed procedure.

5. Conclusions

This paper has presented a procedure to simulate numerically a real experiment, namely the unnotched Iosipescu test. The work is based on the simulation of the experimental process by FEM and the reconstruction of synthetic images simulating a CCD camera recording. The grid method was used to evaluate the displacement and the strain field was obtained by differentiation. The main objective was to reproduce as accurately as possible all the features that characterize a real test. A failure criterion was introduced to determine the maximum applicable load, the effect of the spatial resolution, the minimum grid size, the effect of noise and the influence of missing data were taken into account.

Simulated experiments represent a powerful tool to design an optimal experimental set-up, since all the characteristics can be easily varied. In the present case they were used to optimize the free length and the fibre angle of the specimen for four composite materials. The VFM was used to identify the constitutive parameters and a cost function was introduced to evaluate the error and find the best set of design variables.

The obtained results appear reasonable and in line with the experiments conducted on similar materials with the Iosipescu test. This gives a first confirmation of the effectiveness of the adopted procedure.

The main outcomes from the present study are as follows.

- It has been demonstrated that it is possible to numerically simulate, in a realistic way, an experimental test which uses full-field measurements to identify the material properties of composites. Simulated experiments represent a useful tool to improve the design of actual tests;

- the spatial resolution of the measurement technique plays an important role in the parameter identification. In designing experiments, it is advisable to use specimen shapes that approach the aspect ratio of the CCD chip;

- a high anisotropy has a detrimental influence on the identification in terms of global error, however it influences less the shape of the cost function and the choice of the optimal design variables. As a consequence, the same test configuration can be efficiently used to test different types of composites;

- the necessity of introducing smoothing in the identification depends on the amount of noise. For a given specimen configuration, smoothing becomes necessary beyond a certain noise threshold which can be evaluated with the proposed procedure;
- using the unnotched Iosipescu test and the VFM, the data measured close to the edges of the specimen bear a great importance in the parameter identification. A measurement technique that allows to reduce the missing data at the edges will considerably improve the reliability of the identification.

In the future, the idea is to use the present procedure to design automatically more complex specimen shapes, that, for example, will be less sensitive to the missing data at the edges. Other full-field techniques, for instance digital image correlation, can be introduced in the procedure. Finally, to have a definitive check of the effectiveness of the developed procedure, a thorough experimental study is needed to validate the numerical optimization.

6. References

Avril, S., Bonnet, M., Bretelle, A.-S., Grédiac, M., Hild, F., Ienny, P., Latourte, F., Lemosse, D., Pagano, S., Pagnacco, E., Pierron, F., 2008a. Overview of identification methods of mechanical parameters based on full-field measurements. Exp. Mech. 48, 381–402.

Avril, S., Feissel, P., Pierron, F., Villon, P., 2008b. Estimation of the strain field from full-field displacement noisy data. Revue Européenne de Mécanique Numérique 17 (5-7), 857–868.

Avril, S., Feissel, P., Pierron, F., Villon, P., 2010. Comparison of two approaches for differentiating full-field data in solid mechanics. Meas. Sci. Technol. 21 (1), 015703 (11 p.).

Avril, S., Ferrier, E., Hamelin, P., Surrel, Y., Vautrin, A., 2004a. A full-field optical method for the experimental analysis of reinforced concrete beams repaired with composites. Compos. Part A-Appl. S. 35, 873–884.

Avril, S., Grédiac, M., Pierron, F., 2004b. Sensitivity of the virtual fields method to noisy data. Comput. Mech. 34 (6), 439–452.

Avril, S., Vautrin, A., Surrel, Y., 2004c. Grid method: Application to the characterization of cracks. Exp. Mech. 44 (1), 37–43.

Bornert, M., Brémand, F., Doumalin, P., Dupré, J.-C., Fazzini, M., Grédiac, M., Hild, F., Mistou, S., Molimard, J., Orteu, J.-J., Robert, L., Surrel, Y., Vacher, P., Wattrisse, B., 2009. Assessment of digital image correlation measurement errors: methodology and results. Exp. Mech. 49, 353–370.

Bui, H. D., Constantinescu, A., Maigre, H., 2004. Numerical identification of linear cracks in 2d elastodynamics using the instantaneous reciprocity gap. Inverse Problems 20, 993–1001.

Chalal, H., Avril, S., Pierron, F., Meraghni, F., 2006. Experimental identification of a nonlinear model for composites using the grid technique coupled to the virtual fields method. Compos. Part A-Appl. S. 37 (2), 315–325.

Claire, D., Hild, F., Roux, S., 2004. A finite element formulation to identify damage fields: the equilibrium gap method. Int. J. Numer. Methods Eng. 61, 189–208.

Cooreman, S., Lecompte, D., Sol, H., Vantomme, J., Debruyne, D., 2008. Identification of mechanical material behavior through inverse modeling and DIC. Exp. Mech. 48 (4), 421–433.

Geymonat, G., Pagano, S., 2003. Identification of mechanical properties by displacement field measurement: a variational approach. Meccanica 38, 535–545.

Giraudeau, A., Pierron, F., 2005. Identification of stiffness and damping properties of thin isotropic vibrating plates using the virtual fields method. theory and simulations. J. Sound. Vib. 284, 757–781.

Grédiac, M., 2004. The use of full-field measurement methods in composite material characterization: interest and limitations. Compos. Part A-Appl. S. 35, 751–761.

Grédiac, M., Pierron, F., 2006. Applying the virtual fields method to the identification of elasto-plastic constitutive parameters. Int. J. Plasticity 22, 602–627.

Grédiac, M., Pierron, F., Avril, S., Toussaint, E., 2006. The virtual fields method for extracting constitutive parameters from full-field measurements: a review. Strain 42, 233–253.

Grédiac, M., Toussaint, E., Pierron, F., 2002a. Special virtual fields for the direct determination of material parameters with the virtual fields method. Part 1. Principle and definition. Int. J. Solids Struct. 39, 2691–2705.

Grédiac, M., Toussaint, E., Pierron, F., 2002b. Special virtual fields for the direct determination of material parameters with the virtual fields method. Part 2. Application to in-plane properties. Int. J. Solids Struct. 39, 2707–2730.

Grédiac, M., Vautrin, A., 1990. A new method for determination of bending rigidities of thin anisotropic plates. J. Appl. Mech. 57, 964–968.

Haddad, R., Akansu, A., 1991. A class of fast Gaussian binomial filters for speech and image processing. IEEE T. Signal. Proces. 39, 723–727.

Kajberg, J., Lindkvist, G., 2004. Characterisation of materials subjected to large strains by inverse modelling based on in-plane displacement fields. Int. J. Solids Struct. 41, 3439–3459.

Latourte, F., Chrysochoos, A., Pagano, S., Wattrisse, B., 2008. Elastoplastic behavior identification for heterogeneous loadings and materials. Exp. Mech. 48 (4), 435–449.

Le Magorou, L., Bos, F., Rouger, F., 2002. Identification of constitutive laws for wood-based panels by means of an inverse method. Compos. Sci. Technol. 62, 591–596.

Lecompte, D., Smits, A., Sol, H., Vantomme, J., Van Hemelrijck, D., 2007. Mixed numerical-experimental technique for orthotropic parameter identification using biaxial tensile tests on cruciform specimens. Int. J. Solids Struct. 44 (5), 1643–1656.

Meuwissen, M. H. H., Oomens, C. W. J., Baaijens, F. P. T., Petterson, R., Janssen, J. D., 1998. Determination of the elasto-plastic properties of aluminium using a mixed numerical-experimental method. J. Mater. Process. Tech. 75, 204–211.

Moulart, R., Avril, S., Pierron, F., 2006. Identification of the through-thickness rigidities of a thick laminated composite tube. Compos. Part A-Appl. S. 37, 326–336.

Moulart, R., Rotinat, R., Pierron, F., 2009. Full-field evaluation of the onset of microplasticity in a steel specimen. Mech. Mater. 41 (11), 1207–1222.

Moulart, R., Rotinat, R., Pierron, F., Lerondel, G., 2007. On the realization of microscopic grids for local strain measurement by direct interferometric photolithography. Opt. Laser Eng. 45 (12), 1131–1147.

Orteu, J.-J., Garcia, D., Robert, L., Bugarin, F., 2006. A speckle-texture image generator. In: Proceedings of the Speckle'06 international conference. Nîmes, France.

Pierron, F., 1994. New Iosipescu fixture for the measurement of the in-plane shear modulus of laminated composites: design and experimental procedure. Technical Report 940125 - Available on demand to the author, Ecole des Mines de Saint-Etienne.

Pierron, F., 1998. Saint-Venant effects in the Iosipescu specimen. J. Compos. Mater. 32 (22), 1986–2015.

Pierron, F., Grédiac, M., 2000. Identification of the through-thickness moduli of thick composites from whole-field measurements using the Iosipescu fixture: theory and simulations. Compos. Part A-Appl. S. 31, 309–318.

Pierron, F., Vert, G., Burguete, R., Avril, S., Rotinat, R., Wisnom, M., 2007. Identification of the orthotropic elastic stiffnesses of composites with the virtual fields method: sensitivity study and experimental validation. Strain 43 (3), 250–259.

Piro, J.-L., Grédiac, M., 2004. Producing and transferring low-spatial-frequency grids fo measuring displacement fields with moiré and grid methods. Exp. Tech. 28, 23–26.

Rossi, M., Broggiato, G. B., Papalini, S., 2008. Application of digital image correlation to the study of planar anisotropy of sheet metals at large strains. Meccanica 43 (2), 185–199.

Soden, P. D., Hinton, M. J., Kaddour, A. S., 1998. Comparison of the predictive capabilities of current failure theories for composite laminates. Compos. Sci. Technol. 58, 1225–1254.

Soden, P. D., Kaddour, A. S., Hinton, M. J., 2004. Recommendations for designers and researchers resulting from the world-wide failure exercise. Compos. Sci. Technol. 64, 589–604.

Surrel, Y., 1994. Moiré and grid methods: a signal-processing approach. In: Interferometry '94: photomechanics, SPIE. Vol. 2342.

Surrel, Y., 1996. Design of algorithms for phase measurements by the use of phase-stepping. Appl. Optics 35, 51–60.

Surrel, Y., 1997. Design of phase-detection algorithms insensitive to bias modulation. Applied Optics 36, 805–807.

Surrel, Y., 1999. Photomecanics. Springer Berlin, Ch. Fringe analysis, pp. 57–104.

Syed-Muhammad, K., Toussaint, E., Grédiac, M., Avril, S., Kim, J., 2009. Characterization of composite plates using the virtual fields method with optimized loading conditions. Compos. Struct. 85, 70–82.

Tsai, H. W., Hahn, H. T., 1980. Introduction to composite materials. Techonomic Publishing Company, Inc.

Vanderplaats, G. N., 1984. Numerical optimization techniques for engineering design: with applications, Chapter 2. McGraw-Hill New York.

Xavier, J., Avril, S., Pierron, F., Morais, J., 2007. Novel experimental approach for the characterisation of the LR stiffnesses of clear wood using a single specimen. Holzforschung 61, 573–581.

Xavier, J., Avril, S., Pierron, F., Morais, J., Marinescu, M., 2005. Identification of clear wood orthotropic stiffness using full-field measurements. In: European Mechanics of Materials Conference (EMMC8): material and structural identification from full-field measurements, 13-15 September, Cachan, France.

Zinoviev, P., Grigoriev, S. V., Lebedeva, O. V., Tairova, L. R., 1998. Strength of multilayered composites under plane stress state. Compos. Sci. Technol. 58, 1107–1124.

Zinoviev, P. A., Lebedeva, O. V., Tairova, L. P., 2002. Coupled analysis of experimental and theoretical results on the deformation and failure of laminated composites under a plane state of stress. Compos. Sci. Technol. 62, 11711–24.